Materials & Design 231 (2023) 112037

Contents lists available at ScienceDirect

Materials & Design

journal homepage: www.elsevier.com/locate/matdes

# Texture components and magnetic properties of laser powder bed fusion fabricated near grain-oriented and near non-oriented silicon steel

Fanbo Meng [a], Sheng Huang [b], Kwang Boon Lau [c], You Zhou [a], Yuheng Deng [d], Pei Wang [c,e], Xiaojun Shen [a], Christopher H.T. Lee [a,*]

[a] School of Electrical and Electronic Engineering, Nanyang Technological University, 50 Nanyang Avenue, Singapore 639798, Singapore
[b] School of Mechanical and Aerospace Engineering, Nanyang Technological University, 50 Nanyang Avenue, Singapore 639798, Singapore
[c] Institute of Materials Research and Engineering (IMRE), Agency for Science Technology and Research (A*STAR), 2 Fusionopolis Way, Innovis #08-03, Singapore 138634, Singapore
[d] School of Materials Science and Engineering, Nanyang Technological University, 50 Nanyang Avenue, Singapore 639798, Singapore
[e] Engineering Cluster, Singapore Institute of Technology, Singapore 519961, Singapore

## HIGHLIGHTS

- Near grain-oriented and near non-oriented Fe-3.5 wt.%Si were fabricated for the first time via laser powder bed fusion.
- The relationship between processing parameters, microstructure, and magnetic properties was established.
- Texture components and their formation mechanism were investigated by EBSD and the morphology of molten pool, respectively.
- Effect of texture components and defects on magnetization process, permeability, and magnetic flux density was discussed.

## GRAPHICAL ABSTRACT

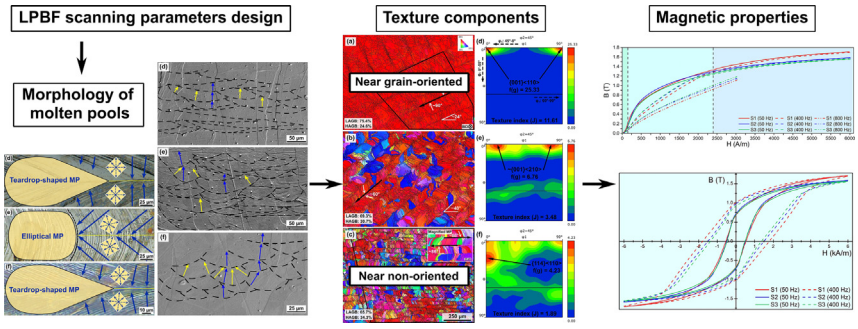


## ARTICLE INFO

*Article history:*
Received 10 March 2023
Revised 6 May 2023
Accepted 22 May 2023
Available online 26 May 2023

*Keywords:*
Additive manufacturing
Silicon steel
Texture
Magnetic properties
Electron backscatter diffraction (EBSD).

## ABSTRACT

Silicon steel is a widely used soft magnetic material that requires different texture components for different applications, typically classified as grain-oriented or non-oriented. However, the methods of fabricating such types of silicon steel via laser-powder bed fusion (LPBF) have not been fully investigated. In this study, near grain-oriented and near non-oriented Fe-3.5 wt.%Si silicon steel is fabricated using LPBF by controlling processing parameters. Different textures are investigated using electron backscatter diffraction (EBSD), and the morphology of the molten pool is characterized by optical microscopy (OM) and scanning electron microscopy (SEM). Magnetic properties are measured with alternating current (AC) method. The results show that reducing both the linear energy density (LED) and laser power leads to a change in the side morphology of the molten pool from large, flat, and well-overlapped to small, protuberant, and less-overlapped, resulting in an extremely strong θ-fiber texture or a random distribution of grain orientations, respectively. Additionally, reducing both the laser power and scanning speed causes the top morphology of the molten pool to change from teardrop to elliptical shape at the trailing edge, resulting in a shift in the angle between the ⟨001⟩ of grains in the θ-fiber texture and the scanning direction from 45° to 30°. Samples with fewer defects (i.e., larger grain size and fewer pores) and a larger area fraction of ⟨001⟩//H exhibit higher permeability, although this superiority is not so significant due to

* Corresponding author at: S2-B2c-101, School of Electrical and Electronic Engineering, Nanyang Technological University, 50 Nanyang Ave, Singapore 639798, Singapore.
*E-mail address:* chtlee@ntu.edu.sg (C.H.T. Lee).

https://doi.org/10.1016/j.matdes.2023.112037

residual stress and high dislocation in the as-built samples. This study provides insight into the relationship between processing parameters, texture evolution, and magnetic properties in LPBFed silicon steel.


## 1. Introduction

With the rapid growth of the electric vehicle (EV) industry, the power system in EVs requires better motors with higher power density, reduced volume, new electromagnetic design, and integration of electronics, among other things. Consequently, many new motor designs have emerged in recent years to meet these requirements [1–3]. Nevertheless, the complexity of a motor's design has to be reduced to meet the limitations of conventional manufacturing techniques, which in turn limits the resulting performance of the motor [4–6]. In response to this, laser-powder bed fusion (LPBF), as an additive manufacturing (AM) technique, has been considered a promising candidate due to its significant advantage in fabricating objects with intricate structures [7–11]. Since most of these new structures are designed for the iron core, which is the most important part of the motor and is usually made of soft magnetic materials, it is necessary to investigate the microstructure and magnetic properties of LPBFed soft magnetic materials before building the AMed motors.

Soft magnetic materials with a combination of high permeability ($\mu$), low coercivity ($H_c$), large saturation magnetization ($M_s$), and high Curie temperature ($T_c$) are highly desirable [12–14]. These properties depend on both intrinsic material properties, such as magneto-crystalline anisotropy constant and magnetostriction coefficient, and microstructure features, such as texture and defects. In LPBF research, intrinsic material properties are considered during phase transformations, especially the ordering-disordering transformation, due to the high cooling rate involved in the process [15,16]. According to the grain size dependence of coercivity and permeability (GSDCP) theory, when the grain size exceeds the domain wall width, the coercivity decreases and permeability increases with the increase of grain size [17–21]. Defects, precipitates, impurities, and residual stress act as obstructions hindering the domain wall movement during magnetization, leading to a deterioration of soft magnetic properties, such as larger coercivity and lower permeability [12–14]. Crystal orientation also affects permeability; more grains with their easy axis (such as $\langle 001 \rangle$ in BCC) parallel to the magnetic field lead to higher permeability of the material [12–14]. Generally, an ordered phase with a large grain size, fewer defects and precipitates, and good texture (easy axis parallel to the magnetic field) is preferred to achieve good soft magnetic properties.

Of the common soft magnetic materials, which include Fe-Si alloy, Fe-Co alloy, Fe-Ni alloy, amorphous and nanocrystalline alloys, and soft magnetic composites (SMCs), Fe-Si alloy (i.e., silicon steel/electrical steel) is most widely used in the fabrication of the iron core of the motors due to its balance between electromagnetic performance and price [12–14,22–24]. However, although much research has been carried out to investigate the microstructure and properties of materials fabricated by LPBF, almost all of these studies focus on the structural materials (such as 316L stainless steel, Ti alloys, Al alloys, etc.) and their mechanical properties [25–42]. While studies on LPBF-manufactured soft magnetic materials and their magnetic performance are rare, some research has been conducted to explore these properties. For instance, Mohamed et al. [43] demonstrated that tilting the building orientation of LPBFed NiFeMo-based alloy to align the easy axes along the building direction (BD) improved the shielding factors (SF) in both normal and transverse directions with respect to the BD. The magnetic shielding properties were further improved 60–100-fold by hot isostatic pressing (HIP) and heat treatment (HT), which relieved stress, consolidated gas pores, and caused recrystallization and grain growth. The highest soft magnetic properties were achieved by tilting the building orientation at 35°, resulting in $M_s$ = 637 kA/m, $H_c$ = 195 A/m, $SF_{axial}$ = 592%, and $SF_{trans}$ = 887%. Moreover, Liogas et al. [16] showed that the quasi-static magnetic properties of HTed LPBFed Co-Fe alloys depend on both the degree of structural ordering and the grain size. Through optimization of the HT, they achieved a fully ordered B2 (CsCl) structure with lower magneto-crystalline anisotropy, higher lattice constant, and higher magnetic saturation polarization, as well as a larger grain size of which influence on $H_c$ and $\mu$ is well matched with GSDCP theory. The resulting LPBFed Co-Fe alloy exhibited noteworthy soft magnetic properties with $\mu_{max}$ = 8197, $H_c$ = 112 A/m, $B_r$ = 1.75 T, and $B_{5000}$ = 2.28 T. These values were superior to those of commercial Co-Fe grades such as HIPERCO® 50 A ($\mu_{max}$ = 3350, and $H_c$ = 209 A/m) [43] and VACOFLUX 50 ($\mu_{max}$ = 7000, and $H_c$ = 100 A/m) [44].

In terms of Fe-Si alloys, several studies have explored the impact of LPBF energy input on the microstructure and magnetic properties of Fe-Si alloys. Garibaldi et al. [45,46] found that higher linear energy density ($LED = \frac{P}{v}$) led to longer grains in the side and top planes and increased the depth of the molten pool, resulting in a shift from crystallographic $\langle 001 \rangle$ fiber texture to cube texture. The best magnetic properties were observed at 280 J/m, with maximum relative permeability, coercivity, and power losses of 5300, 49 A/m, and 4 W/kg, respectively. Gao et al. [47] investigated the effect of LED on the surface morphology, microstructure, and magnetic properties of Fe-Si, discovering that while higher LED increased surface flatness and grain size, the best magnetic performance was achieved at an optimal LED due to changes in microhardness. Plotkowski et al. [48,49] examined the influence of process conditions and sample geometry on magnetic performance, demonstrating that a thin wall sample with a cross-sectional Hilbert curve design reduced eddy current loss. They also built a transformer core based on this geometry, which showed higher power loss than Goss-oriented steel but performed comparably to or better than the conventional non-oriented sheet.

In the existing research on LPBFed silicon steel, the relationship between processing conditions, texture, and magnetic properties was discussed. However, there was no effort to achieve parts with varying texture components, i.e., fiber texture and random texture, and their effects on the magnetic performance of LPBFed silicon steel have not been studied. It is good to note that different applications of silicon steel have varying requirements for the specific texture characteristics or components. Therefore, the ability to obtain these different texture components is a key research focus in conventional silicon steel manufacturing [50–58]. Specifically, silicon steel with the $\{110\}\ \langle 001 \rangle$ Goss texture (i.e., grain-oriented silicon steel) is used to manufacture transformers, while the iron core of the motor is fabricated with silicon steel with a relatively random distribution of grain orientations (i.e., non-oriented silicon steel), suitable for magnetization directions that are unidirectional and rotated when in-service. Therefore, in this work, methods of obtaining different texture components are explored, and the reasons behind such texture evolution are studied. Additionally, the influence of different microstructures (including tex-

ture components) on the magnetic properties of LPBFed silicon steel is investigated. The results could provide a design reference for LPBFed soft magnetic materials, and hence leading the research on AM techniques to motor development.

## 2. Materials and experiments

### 2.1. Materials

Bulk samples were fabricated via LPBF process using pre-alloyed and spherical gas atomized Fe3.5Si (wt.%) powder (supplied by Coatecs Pte. Ltd.) with powder diameter range of 15 – 53 μm, which morphology and chemical compositions are shown in Fig. 1 and Table 1, respectively.

The LPBF machine (TruPrint 1000, TRUMPF SE + Co. KG) is equipped with a 200 W TRUMPF fiber laser with 1,070 nm wavelength and 30 μm laser beam spot size. Two sample types, namely the quadrangular pillar (5 mm (L) × 5 mm (W) × 50 mm (H)) and the ring (26 mm (ID) × 31.5 mm (OD) × 8 mm (H)), were fabricated for microstructural characterization and magnetic property testing, respectively. Constant layer thickness (t) of 20 μm was employed, with four sets of laser power (P), scanning speed (ν), and hatching space (h) combinations for the LPBF fabrication process. Island scanning strategy with an island size of 5 mm × 5 mm was used, in addition to a scan rotation of 67° and island shift of 2.5 mm in both X and Y directions after every successive layer. The process parameter combinations, along with the associated porosity levels are listed in Table 2. The porosity levels (%) of the samples were measured based on microscopy techniques on a relatively large area (>2 $mm^2$) for each sample. The representative cross-sectional images of each sample can be seen in Fig. S1.

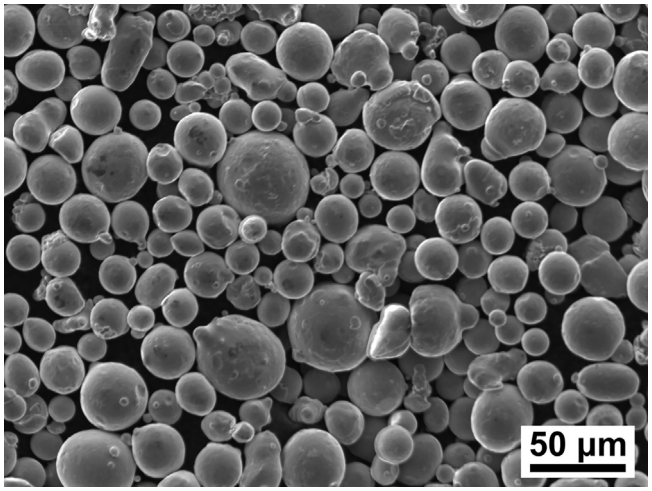


**Fig. 1.** SEM image of the silicon steel powder size and morphology.

The laser parameters were chosen by varying the laser power and LED at two distinct levels while keeping VED constant (208 J/$mm^3$), which is defined as $\frac{P}{vht}$[59–62]. As such, LED of S1, S2 (0.375 J/mm) are higher than S3, S4 (0.125 J/mm). Meanwhile, the laser power employed for S1 and S4 (both 150 W) is higher than for S2 (60 W) and S3 (50 W). The samples were removed from the base plate with electrical discharge machining (EDM) upon fabrication.

### 2.2. Microstructure characterization

The top surface of the as-built samples was observed using an optical microscope (DSX1000 Digital Microscopes) to capture the shape of the boundary at the trailing edge of the molten pool. The samples were then mounted in conductive resin and prepared using standard metallographic techniques and oxide polishing suspension to obtain a mirror surface finish. In some cases, the polished samples were additionally etched with 3% Nital for approximately 60 s to observe the molten pool boundaries. Microstructural analysis was performed using a field emission scanning electron microscope (FESEM, JEOL JSM-7800F PRIME) on the prepared samples. The chemical compositions of the as-printed solid parts were measured with Energy-dispersive X-ray spectroscopy (EDS), which is equipped on FESEM. The grain orientation map was obtained using an electron backscattered diffraction (EBSD) detector attached to the FESEM, with the step size of 2.34 μm and 1.17 μm employed in Fig. 3 and other EBSD maps, respectively. The AZtecCrystal software (Oxford Instruments NanoAnalysis) was used for the post-processing of the EBSD data. Unless otherwise specified, grain boundaries were defined with a cutoff misorientation of 15°. To investigate the crystal orientation of grains inside the molten pools, orientation distribution function (ODF) calculation was performed in a restricted area with parallelly arranged scanning tracks. Coordinate rotation was performed to simplify the data interpretation, with the X0-axis (rolling direction (RD)) and Y0-axis (transverse direction (TD)) respectively aligned with the molten track scanning direction (SD) and its width direction (WD). The schematic to show the different axes and cross sections of the bulk sample and directions of a molten pool can be seen in Fig. 2 (a) and (b), respectively.

### 2.3. Dynamic magnetic property test

The magnetic tests in this research were conducted according to ASTM standard (A927/A927M – 11) [63]. The as-built ring samples were first thinned from both the outer and inner contours by EDM, and the final size of the ring samples for testing was 30.4 mm × 27.4 mm × 8 mm (length × width × height). Magnetic property measurements were conducted using a MATS-3000 M Hysteresisgraph (HUNAN LINKJOIN TECHNOLOGY CO., LTD.). The alternating current (AC) test mode was selected with a defined maximum

**Table 1**
Chemical compositions (wt.%) of silicon steel powders used for L-PBF.

| Si | C | O | P | S | Fe |
|---|---|---|---|---|---|
| 3.440 | 0.006 | 0.052 | 0.009 | 0.003 | Bal. |

**Table 2**
Processing parameters of LPBF processes associated porosity levels.

| No. | P (W) | ν (mm/s) | h (μm) | LED (J/mm) | VED (J/$mm^3$) | Porosity (%) |
|---|---|---|---|---|---|---|
| S1 | 150 | 400 | 90 | 0.375 | 208 | 0.01 |
| S2 | 60 | 160 | 90 | 0.375 | 208 | 0.15 |
| S3 | 50 | 400 | 30 | 0.125 | 208 | 0.24 |
| S4 | 150 | 1200 | 30 | 0.125 | 208 | 0.09 |

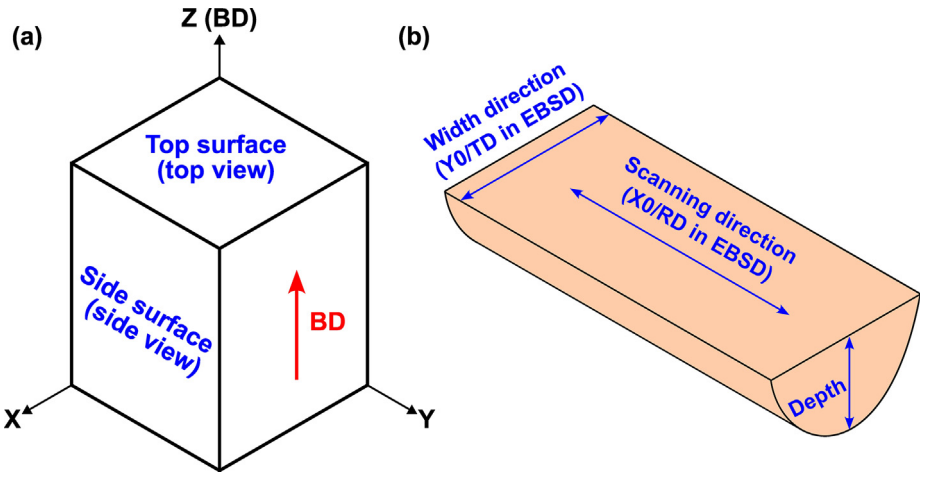


**Fig. 2.** Schematic for (a) the different axes and cross sections of the bulk sample and (b) the different direction indicators in a molten pool.

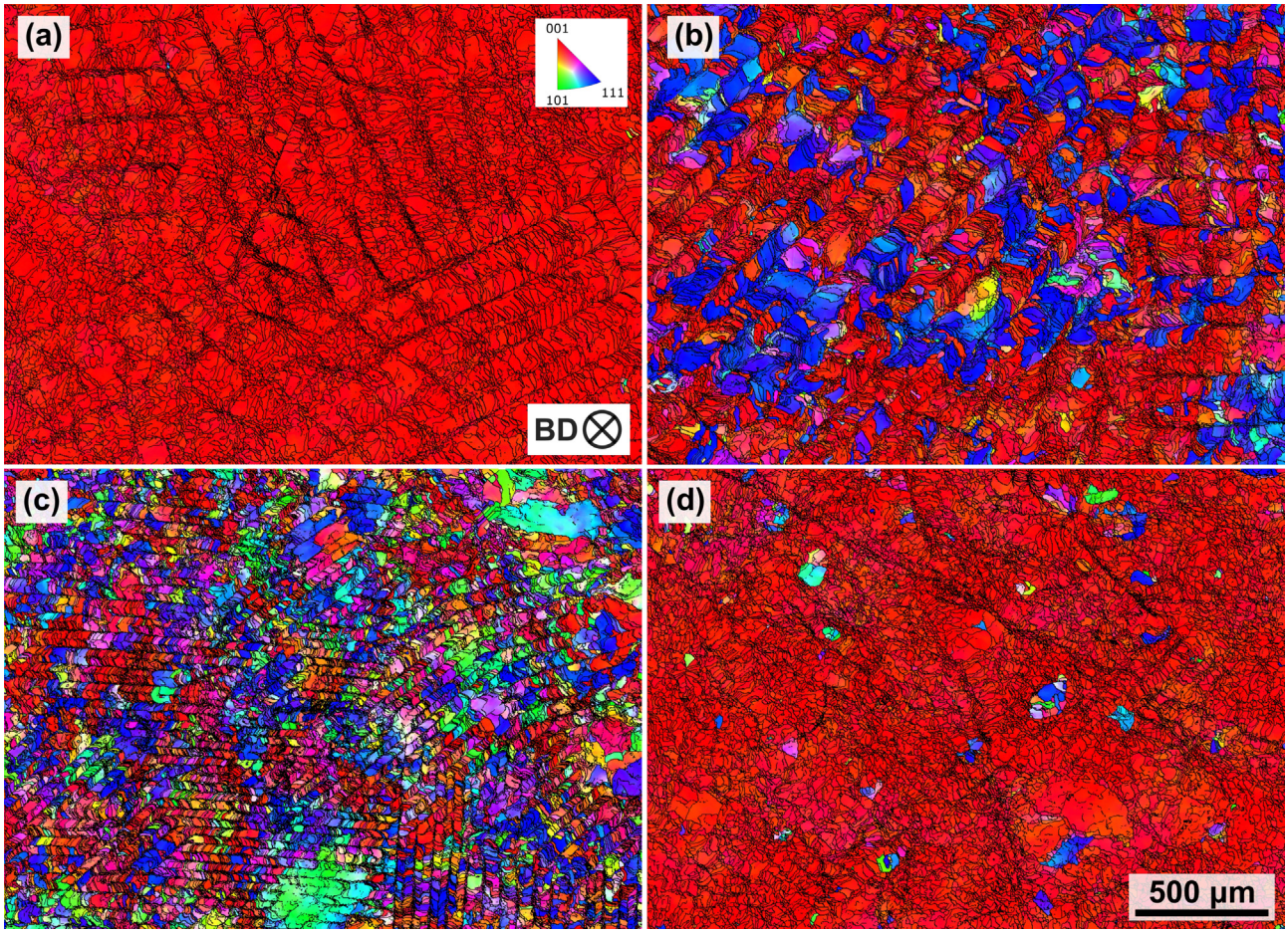


**Fig. 3.** (a)-(d) are the grain orientation maps of samples S1-S4 from the top view, respectively, where IPF-BD coloring is used. Grain boundaries (misorientation > 2°) are represented by black lines. The IPF legend is based on α-Fe (BCC).

magnetic field intensity ($H_m$) and fixed frequency (f). $H_m$ was increased from 50 A/m to 6000 A/m, while the frequency was fixed at 50 Hz, 400 Hz, and 800 Hz. The samples were subjected to primary and secondary windings of 80 and 40 turns, respectively, and were demagnetized before each testing under various AC frequencies. The magnetization curve was obtained by plotting the maximum magnetic flux density ($B_m$) under the corresponding $H_m$.

## 3. Results

### 3.1. Influence of scanning parameters on texture

#### 3.1.1. Overall texture

The chemical compositions of the S1-S4 solid parts were measured with EDS and the results are provided in the supplementary

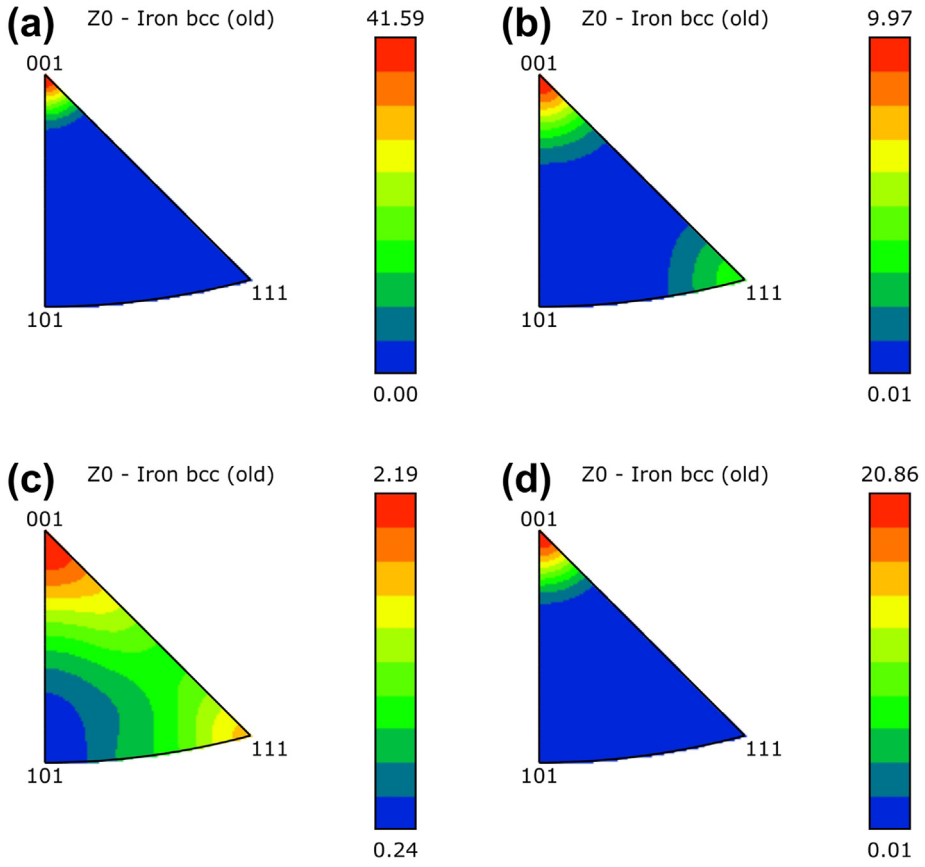


**Fig. 4.** (a)-(d) are the inverse pole figures (IPF) sets of samples S1-S4 in Fig. 3 (a)-(d), respectively, showing the grain orientations with respect to BD.

materials (Table S1 and Fig. S2), which demonstrate that there was no significant change in chemical compositions from the powder to the as-printed solid parts. This indicates that the chemical compositions of the solid parts are consistent with the powder compositions.

Grain orientation maps of samples S1-S4 are presented in Fig. 3, with cross-sections perpendicular to the BD and inverse pole figure (IPF) colored with respect to BD, and their relative IPF sets are shown in Fig. 4. In order to facilitate demonstration of the different textural strengths associated with each sample, IPF sets of S1-S4 with the same scale range can be found in the supplementary information as Fig. S3. Although the VED remained constant, S1-S4 showed different texture characteristics. Strong ⟨001⟩//BD texture, also known as θ-fiber texture, can be observed in Fig. 3 (a) and (d) for S1 and S4, respectively, which were associated with high input laser power (150 W). The MUD values, which quantify the texture strength by varying from 1 (random powder) to infinity (perfect texture or single crystal) [64], were 41.59 and 20.86 for S1 (Fig. 4 (a)) and S4 (Fig. 4 (d)), respectively. By reducing the input laser power to 50–60 W, ⟨111⟩//BD texture appeared in S2 (Fig. 3 (b) and Fig. 4 (b)) and S3 (Fig. 3 (c) and Fig. 4 (c)) and the overall texture strength diminished significantly (MUD ∼ 9.97 for S2 and ∼ 2.19 for S3). It is also good to note that a higher input linear energy density (LED) can be linked to the formation of stronger texture when the laser power was kept at a similar level. This is evident in S1 and S2 (LED ∼ 0.375 J/mm, MUD 41.59 (S1) and 9.97 (S2)) in comparison to S3 and S4 (LED ∼ 0.125 J/mm, MUD ∼ 2.19 (S3) and 20.86 (S4)). Therefore, the combination of low laser power and LED is essential to achieving highly random texture for Fe3.5Si in this study.

To further visualize the grain morphologies, EBSD maps from the side surface of S1-S4 are shown in Fig. 5. The strong θ-fiber texture in S1 and S4 corresponded to straight and through-thickness columnar grains. Meanwhile, the grains in S2 and S3 exhibit a zig-zag feature that is well-related to the weakened texture.

### 3.1.2. Texture of parallel scan tracks

To draw further insights into the texture formation, the grain growth characteristics with respect to multiple parallel single tracks are observed in this sub-section. Based on Fig. 3 – Fig. 5, it can be observed that S1 and S4 exhibit similar texture characteristics dominated by θ-fiber texture. In contrast, S2 and S3 demonstrate significantly different texture components, of γ- and α-fiber texture, respectively. Therefore, to focus on investigating the specific texture components, only S1-S3 will be considered, as they represent the different texture characteristics observed in the samples.

ODFs of multiple parallel single tracks were calculated from the EBSD data of S1 (Fig. 6 (a)), S2 (Fig. 6 (b)), and S3 (Fig. 6 (c)), shown respectively in Fig. 6 (d), (e), and (f). ODF sets of S1-S3 with the same scale range are included in the supplementary information as Fig. S4. In addition to the texture strength reduction from S1 to S3, as described in the previous section, the appearance of γ- and α- fiber texture is observed. Meanwhile, the ODFs also show an evolution of the most-preferred grain orientation from {001} ⟨110⟩ (i.e., rotated cube texture) to {001} ⟨210⟩ and finally {114} ⟨110⟩, albeit with decreasing domination of the particular grain orientation.

Fig. 7 shows the texture intensity distribution, f(g) along different fiber axes (indicated by the black discontinuous arrows in Fig. 6 (d)). The most preferred grain orientations and texture distribution along different fiber axes shown in Fig. 7 further confirm the findings in the ODF images. A majority of grain in S1 is related to θ-fiber texture and forms a sharp peak at {001} ⟨110⟩ orientation.

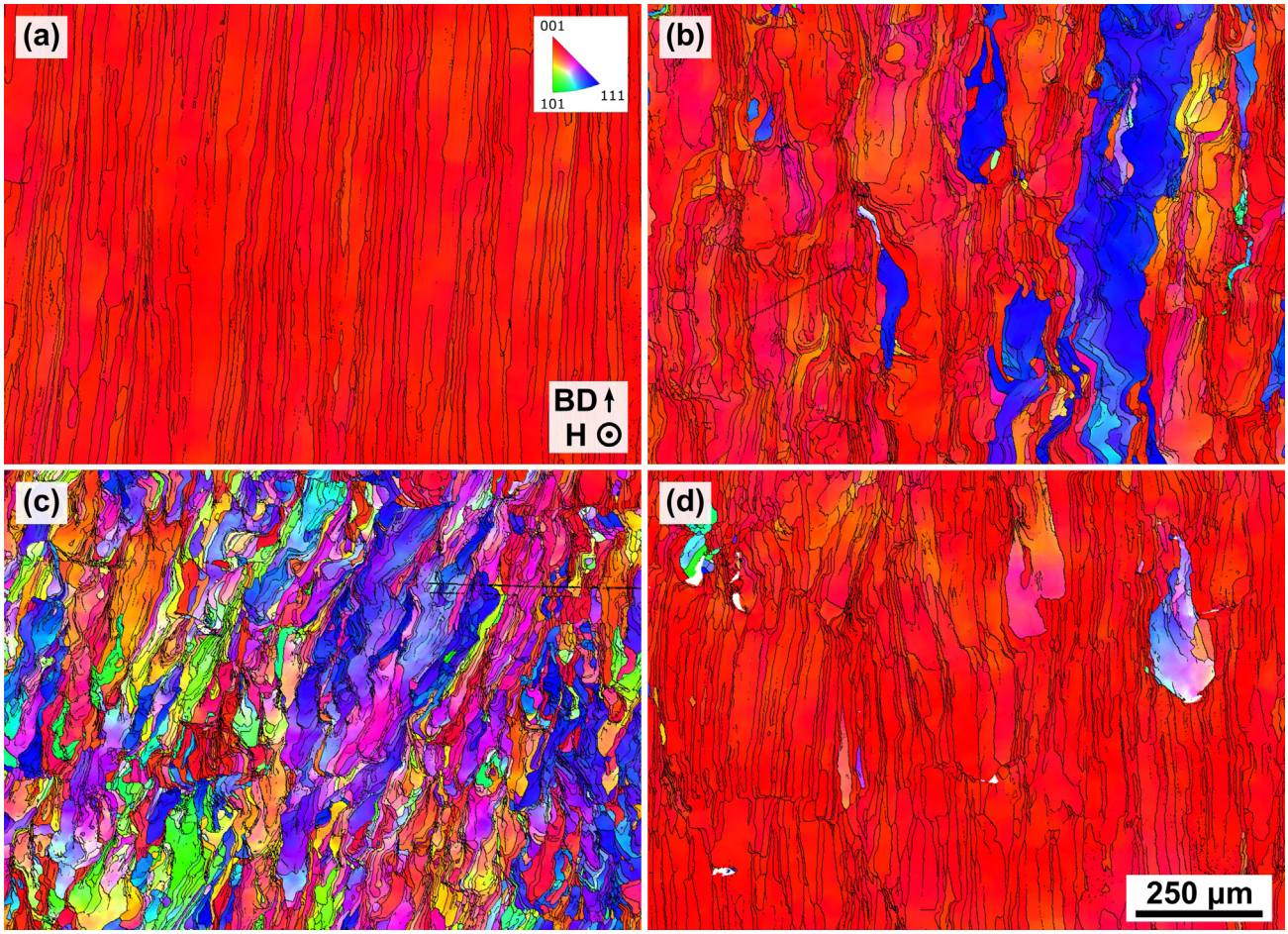


**Fig. 5.** (a)-(d) are the grain orientation maps from the side view of samples S1-S4, respectively, where IPF-BD coloring is used.

In S2, θ-fiber texture is significantly weakened, accompanied by the appearance of γ-fiber texture. S3 has an even distribution along all three fiber axes without obvious undulation, indicating the presence of all θ-, α-, and γ-fiber textures.

The low angle grain boundary (LAGB)/high angle grain boundary (HAGB) ratio and misorientation angle distributions are shown in Fig. 6 and Fig. 8, respectively. Additionally, the misorientation angle distribution for a theoretically random grain distribution is plotted in Fig. 8. The proportion of LAGB reduces as the texture becomes more random, from S1 to S3. As for the misorientation angle distribution, S1 skewed toward low misorientation angles without showing any misorientation angles of >46°. Despite the weak texture in S2, the distribution of the misorientation angle is still far from the theoretical random distribution. In contrast to S1 with dominating misorientations <46°, the misorientation angle in S2 also distribute beyond the theoretical value at >52° region, which is contributed by the high misorientation between γ- and θ-fiber texture. The distribution angle for S3 coincides with the theoretically random distribution, which further affirms the achievement of the random grain orientation in Fe3.5Si via processing parameter tuning.

Since the ⟨001⟩ is the easy axis in silicon steel, understanding ⟨001⟩ of θ-fiber texture with respect to the SD/WD could help dictates the in-plane magnetization ability, which is further beneficial in future planning of laser scanning strategies, especially for engineering in-plane texture in bulk or thin wall samples. Hence, the θ-fiber texture in Fig. 6 (a)-(c) were extracted and visualized on a {001} pole figure (PF) shown in Fig. 9 (a)-(c), respectively. The ⟨001⟩ direction of the θ-fiber texture has varying preferred orientations for samples S1-S3, which are around 45°, 30°, and 40° with respect to SD, respectively. This is illustrated in Fig. 9 (d)-(f) by the unit cells overlaid on EBSD map. It is interesting to note that despite the weak texture in S3, all samples exhibited columnar grain morphology (Fig. 9 (d)-(f)) – evidence of a predominant epitaxial growth regime. This meant that the texture strength of samples in this work is dominated by the molten geometry, instead of the grain growth regime. As shown in Fig. 6 (a)-(c), the angles between the major axis of grains (white arrow) and SD (black arrow) in S1, S2, and S3 are different. The angle in S1 (∼70°-90°) is similar to S3 (∼68°-86°), while the major grain axis in S2 rotates more towards the SD (∼60°). For grains contributing to the θ-fiber texture, the rotation of the grain major axis correlates well with the rotation of crystallographic orientation, prompting a further investigation from the perspective of molten pool geometry.

### 3.2. Dynamic soft magnetic properties

Fig. 10 (a) shows the magnetization curve of S1-S3 under different AC frequencies, and Fig. 10 (b)-(d) compares the magnitude of magnetic flux density (B) of S1-S3 in the initial magnetization region, domain growth region, and domain rotation region, respectively, where these three regions are distinguished with different background color in Fig. 10 (a). Under the same AC frequency, S1 is the easiest to be magnetized while S3 is the hardest, and S2 is only marginally better than S3. On the other hand, increasing the AC frequency will reduce the magnetic flux density of the same

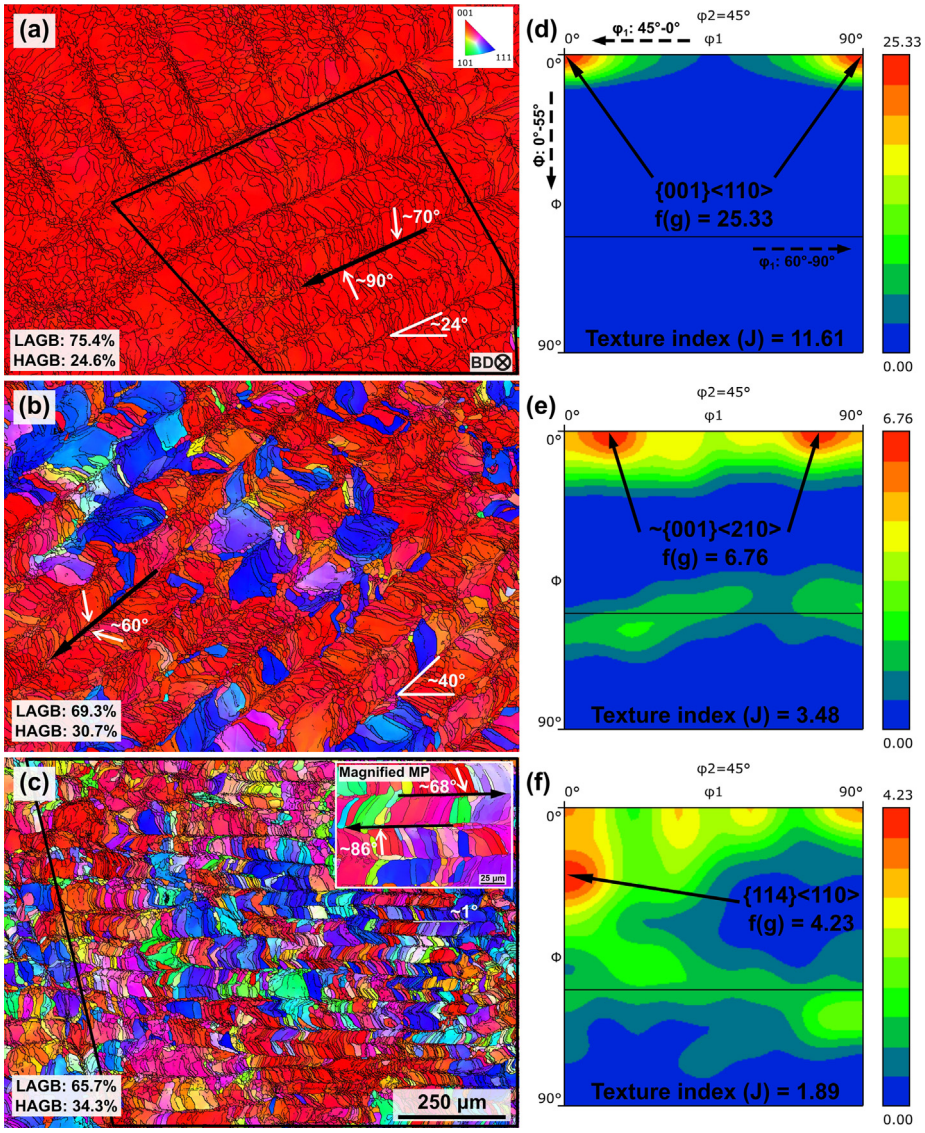


**Fig. 6.** (a)-(c) are the enlarged grain orientation maps of samples S1-S3 from the top view, respectively, where IPF-BD coloring is used. The fraction of low angle grain boundaries (LAGB) and high angle grain boundaries (HAGB) were counted and shown in the lower left corner in (a)-(c). (d)-(f) are $\varphi_2 = 45°$ section of ODF, calculated from the region inside the black frame in (a), the whole (b), and the region inside the black frame in (c), respectively, and the half width of the ODFs is 5°. The black frames are used to restrict the area of data extraction to only those with parallelly arranged scan tracks. The black discontinuous arrows in (d) show the θ-fiber axis, α-fiber axis, and γ-fiber axis, along which the f(g) will be plotted in Fig. 7.

sample under the same external magnetic field, which also translates to a decrease in amplitude permeability. In the domain growth region, a trend reversal of easy magnetization can be observed in the order of S3, S2, and S1, at high AC frequencies of 400 and 800 Hz.

Besides the magnetization curve, the hysteresis loop and other magnetic properties were also investigated under $H_m \sim 6000$ A/m, f = 50 and 400 Hz, as shown in Fig. 11. Fig. 11 (a) illustrated the significant enlargement of the hysteresis area with increasing AC frequency. The results show that S1 is better than both S2 and S3 in both magnetization and demagnetization processes. S1 exhibits the maximum magnetic flux density (~1.7 T) and amplitude permeability (~227.3), but also the largest coercivity and power loss. All S1-S3 performed worse under a higher AC frequency, as evident from the significant increase in coercivity and power loss. Disregarding the poor coercivity, it is important to note that S1 does not have a significant edge over S2 and S3 despite the strong out-of-plane θ-fiber texture, given that the magnetization direction is in-plane.

The increase in AC frequency does not have a notable effect on the maximum flux density and amplitude permeability, but the coercivity, remanence, and power loss increase greatly with the increase of the AC frequency. Nevertheless, the magnetic properties are least affected by the sample type, regardless of the AC frequency. This signifies that there is other texture engineering will be required to improve the in-plane performance of Fe3.5Si magnetic steel.

## 4. Discussion

### 4.1. Microstructure and texture formation

The grain growth mechanism in the studied Fe3.5Si samples is predominantly columnar or epitaxial growth, which is highly dependent on molten pool geometry and the extent of overlapping. To investigate the influence of molten pool characteristics on microstructure and texture formation in samples S1-S3, cross-sections parallel to BD (side view) were examined, as shown in

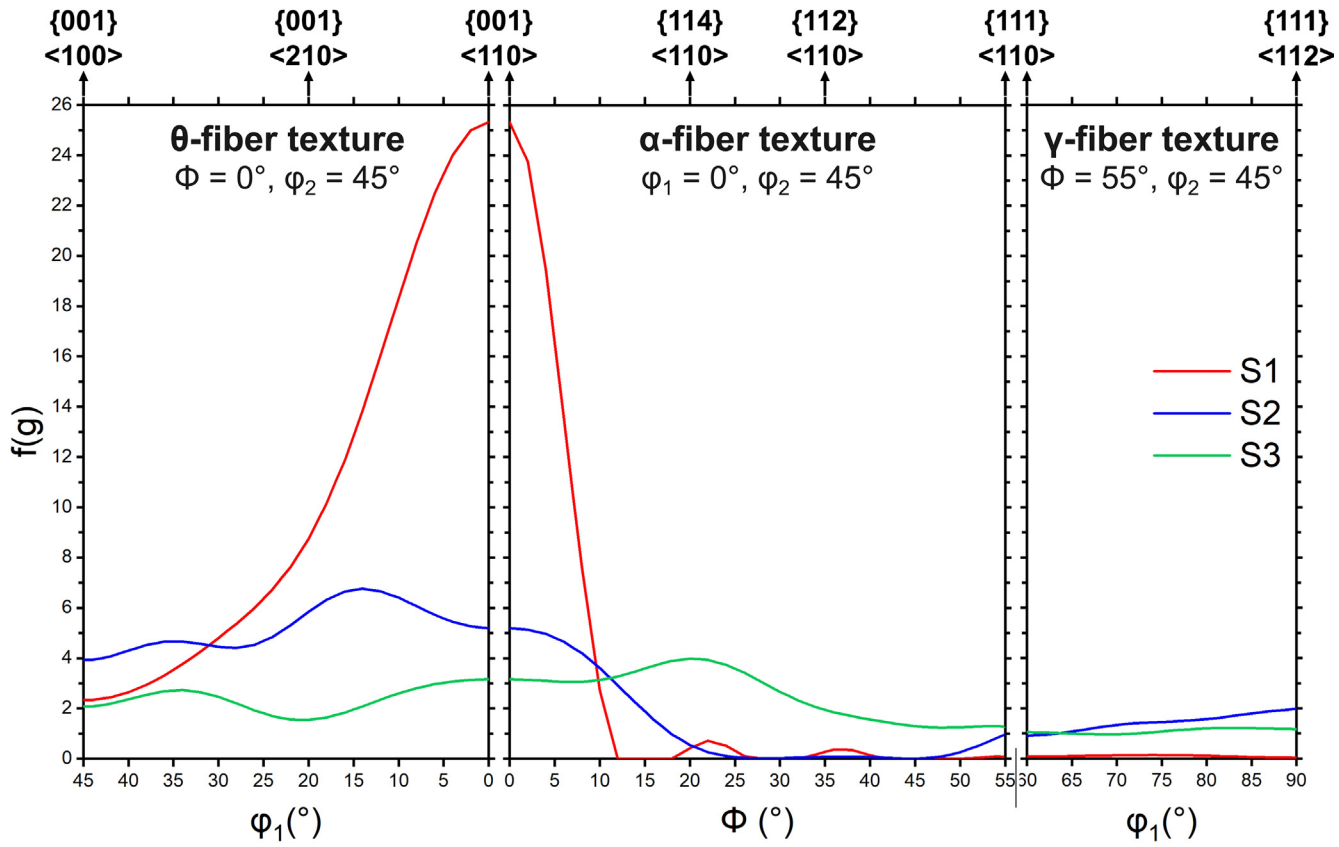


**Fig. 7.** Texture intensity (f(g)) distribution along the θ-fiber axis, α-fiber axis, and γ-fiber axis (black dash arrows in Fig. 6 (d)) in S1-S3.

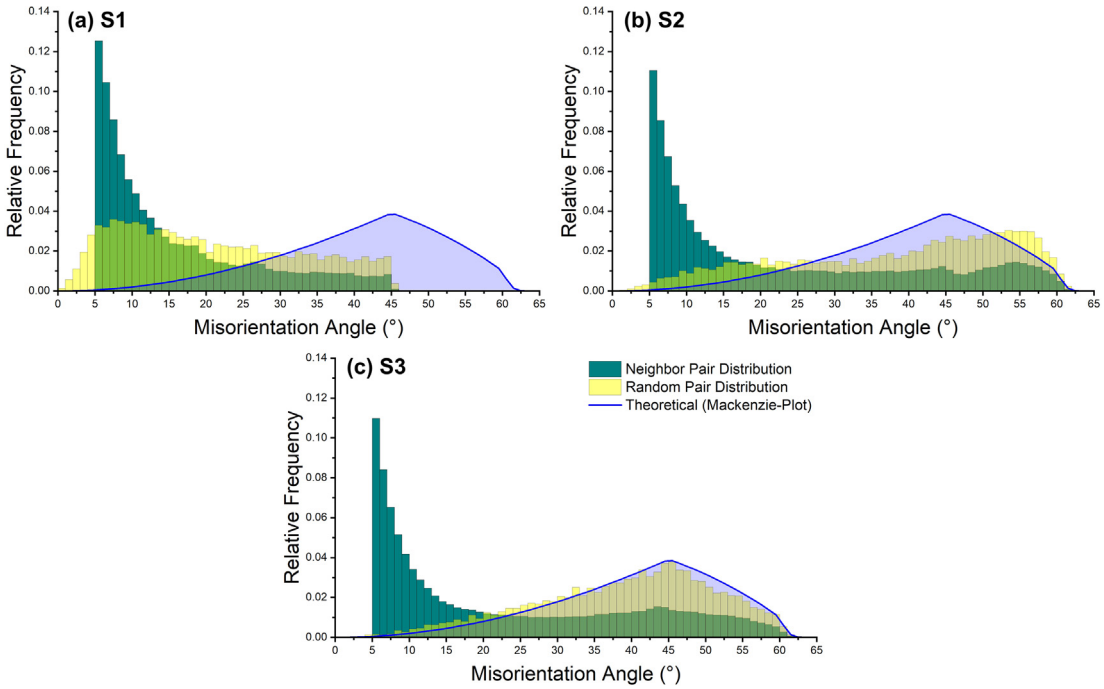


**Fig. 8.** Misorientation angle distribution of (a) S1, (b) S2, and (c) S3, which are extracted from Fig. 3 (a), (b), and (c), respectively.

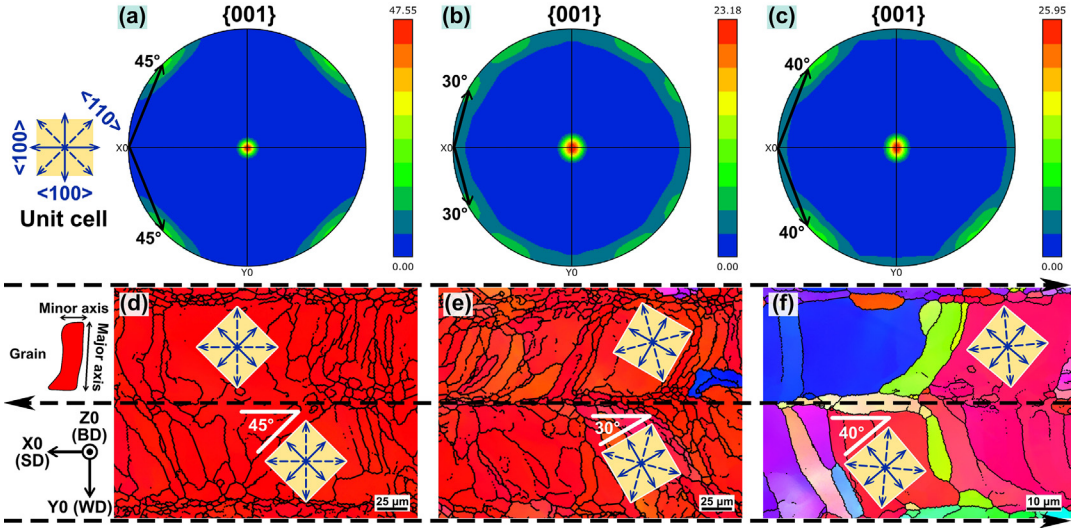


**Fig. 9.** (a)-(c) {001} PFs of S1-S3 calculated from the grains constituting θ-fiber texture in Fig. 6 (a)-(c), respectively. The deviation angle of which is within 10°. (d)-(f) elucidate the grain morphology and representative orientation of grains contributing to θ-fiber texture inside the molten pool of S1-S3, respectively.

Fig. 12. It was observed that the usage of high linear energy density (LED) led to larger molten pools in S1 (Fig. 12(a)) and S2 (Fig. 12(b)) compared to S3 (Fig. 12(c)), which was fabricated with lower LED. Additionally, under the same LED, the slower scanning speed used in S2 allowed for more time for heat dissipation, resulting in a marginally smaller molten pool compared to S1.

The wide and deep molten pool in S1 was found to be beneficial for promoting ⟨001⟩//BD or θ-fiber texture, as it not only allowed for copious overlap between adjacent molten pools (Fig. 12 (a)), but also aided in remelting a large proportion of the previously solidified layer (Fig. 12 (d) and Table 3). In a single layer, the copious overlap of the molten pools ensured that relatively flat molten pool boundaries were retained, as observed in Fig. 12 (d), enabling the epitaxial growth direction (⟨001⟩ ) nearly paralleling BD (yellow arrows in Fig. 12 (d)). Then when the next layer was added, the large proportion of remelting could help "remove" most (may not all) of stray grains growing towards the center of the molten pool, near the top surface of the previously solidified layer (see Fig. 12 (a)). This extensive remelting ensured competitive grain growth, which is dictated by the ⟨001⟩ easy-growth direction in a BCC crystal structure (blue arrow in Fig. 12 (d)), and also promoted the formation of straight columnar grain boundary in Fig. 5 (a). Finally, benefiting from the copious overlapping and large proportion remelting, the strong ⟨001⟩//BD texture (or θ-fiber texture) was formed in S1. Meanwhile, in S2, less adjacent overlapping allows non–⟨001⟩//BD grains to grow, resulting in the appearance of γ-fiber texture (Fig. 12 (b) and (e)).

In contrast, the narrow molten width in S3 significantly reduces the extent of adjacent molten overlap (despite the smaller hatch spacing), thereby promoting epitaxial growth of non–⟨001⟩//BD oriented grains (Fig. 12 (f)). Moreover, an unstable molten pool occurs due to the low LED and power combination, forming uneven and inconsistent surface topology upon solidification (as shown in Fig. 12 (c)). This leads to the preferential ⟨001⟩ grain growth direction in a "random" fashion. Consequently, a weakly textured component can be achieved through the manipulation of scanning strategy. Meanwhile, it should be noted that the porosity levels of S1-S3 are 0.01%, 0.15%, and 0.24%, respectively. Fig. S5 demonstrates that lack-of-fusion pores primarily contribute to the porosity level in S2 and S3, while Fig. 13 shows the interruption of epitaxial growth by the lack-of-fusion defect. Thus, in addition to the molten pool geometry, the lack of fusion pores in S2 and S3, which interrupted the ⟨001⟩ epitaxial growth, can also contribute to the development of non–⟨001⟩//BD grains and the introduction of random structures.

Understanding the characteristics of grain growth with respect to SD is crucial for controlling in-plane texture. The top surface characteristics of the solidified molten pool were investigated from the top view, as shown in Fig. 14 (a)-(c). Two types of molten pool shapes were observed based on the surface ripples: teardrop shape for S1 (Fig. 14 (d)) and S3 (Fig. 14 (f)), and elliptical shape for S2 (Fig. 14 (e)). The formation of these shapes can be related to the laser power and scanning speed. Kou [65] demonstrated that increasing heat input and welding speed simultaneously could enlarge the weld pool, leading to molten pool shifting from elliptical to teardrop shaped.

The direction perpendicular to the trailing molten pool boundary can be regarded as the direction of maximum thermal gradient, and grain growth typically follows the molten pool boundary in this direction. As a result of having a sharp trailing edge, the major axis of grains in S1 and S3 is oriented almost perpendicularly to the SD and molten centerline. As the molten pool trailing boundary changes from a teardrop to an elliptical shape, the rotation of the preferred orientation of θ-fiber texture can occur, as previously observed in Fig. 9. By understanding the direction of grain growth, the laser scanning strategy, including scanning pattern and scan rotation, can be controlled to achieve the desired in-plane texture. This provides an opportunity to tune magnetization properties in directions other than BD.

### 4.2. Microstructure-magnetic properties correlation

Several microstructural parameters such as the crystal orientation with respect to the direction of the external magnetic field, grain size distribution, and porosity were quantified, to understand the variation of magnetic properties across three samples. The application of the external magnetic field is along the in-plane direction, which is defined as the H direction hereafter. Accordingly, the distribution of crystal orientation along H (Fig. 15) and grain size (Fig. 16) were extracted from the samples' side view (Fig. 5) and top view (Fig. 3), respectively. From S1 to S3, the area fraction of grains with ⟨001⟩//H reduces gradually, while the area fraction of grains with ⟨112⟩//H and ⟨111⟩//H appears and increases significantly. No significant variation of ⟨011⟩//H area

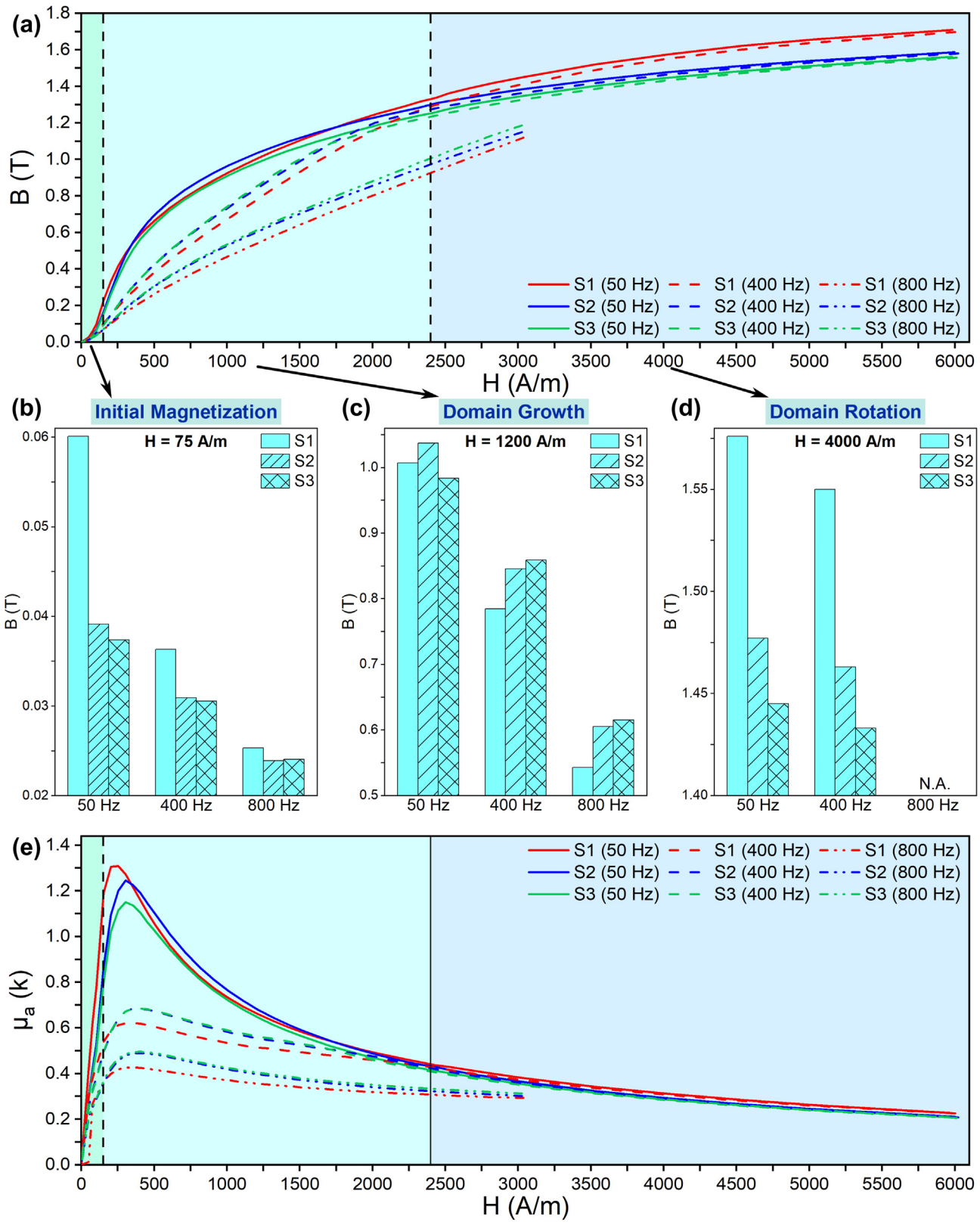


**Fig. 10.** Dynamic soft magnetic properties: (a) Magnetization curves of S1-S3 measured under f = 50 Hz, 400 Hz, and 800 Hz, respectively. The initial magnetization region, domain growth region, and domain rotation region are distinguished with different background colors. (b)-(d) show magnetic flux density of S1-S3 at H = 75 A/m (initial magnetization region), H = 1200 A/m (domain growth region), and H = 4000 A/m (domain rotation region), respectively. (e) amplitude permeability of S1-S3 measured under f = 50 Hz, 400 Hz, and 800 Hz, respectively.

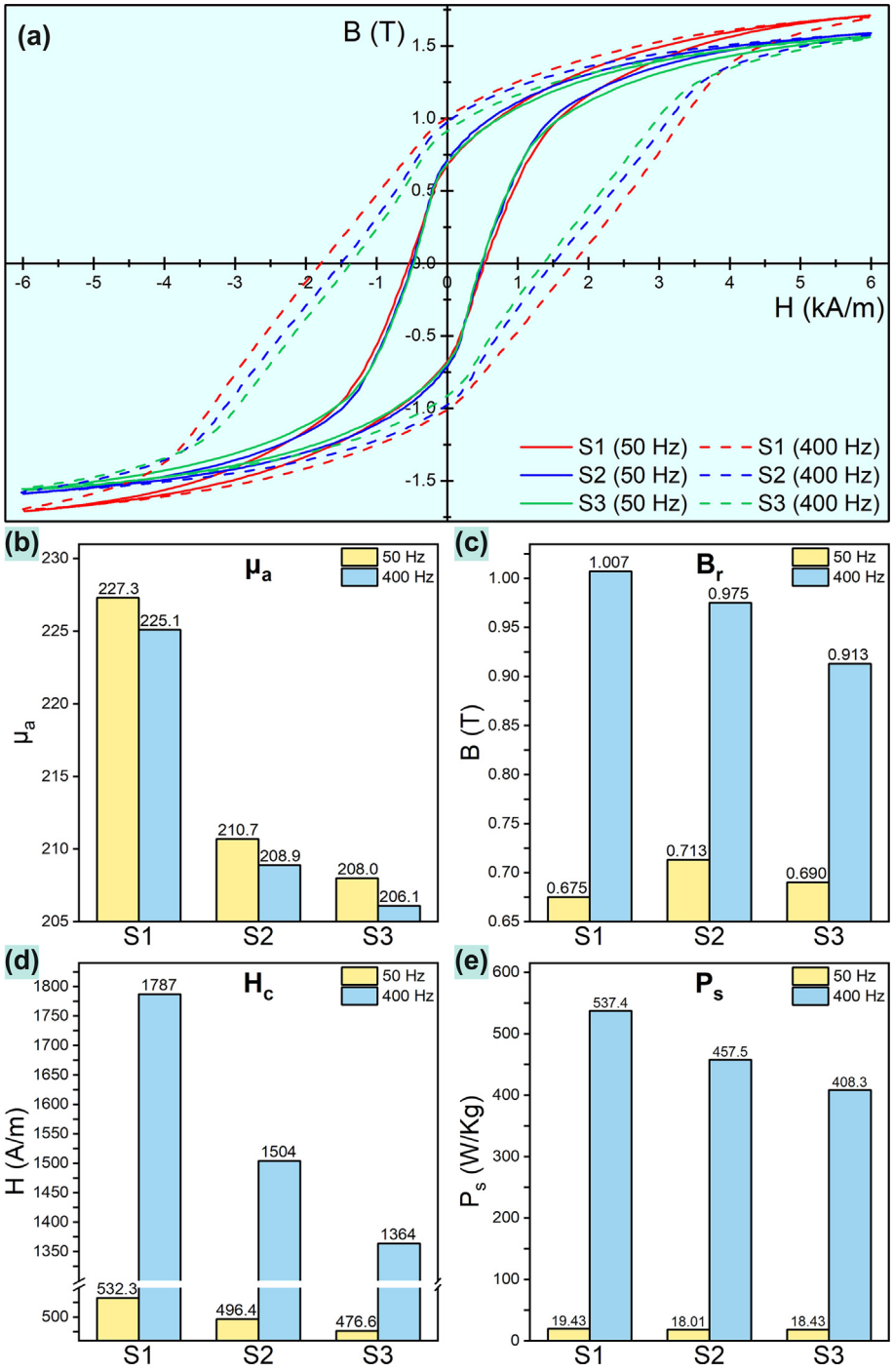


**Fig. 11.** Dynamic soft magnetic properties: (a) Hysteresis loops of S1- S3 measured under f = 50 Hz and 400 Hz, respectively. (b)-(e) show the amplitude permeability ($\mu_a$), remanence ($B_r$), coercivity ($H_c$), and power loss ($P_s$) of S1- S3 from the hysteresis loops in (a).

fraction was found between S1-S3. The grains size in S1 is much larger with the largest grain size over 140,000 $\mu m^2$, while all the grains inside S2 and S3 are less than 28,000 $\mu m^2$. This difference is related to the less dominant texture in S2 and S3, which is a consequence of the less competitive directional grain growth. The relatively significant porosity in S3 (0.24%) may have originated from the unstable molten pool formation, which was a compromise for obtaining the random texture (if desired). The usability of S3 may be challenged depending on its intended application as a structural material or not. It remains a highly desirable conquest to achieve highly dense LPBFed Fe3.5Si with a random texture.

One possible approach to reduce porosity in the printed part is by utilizing HIP as a post-processing technique. For instance, Kang et al. [66] demonstrated successful densification of Fe-Ni-Si alloy fabricated by LPBF through HIP, resulting in equilibrium austenite phases ($Ni_3Si$ and $FeNi_3$) and improved mechanical strength. However, this process also led to an increase in coercivity, which should be taken into account during the design of electric machines.

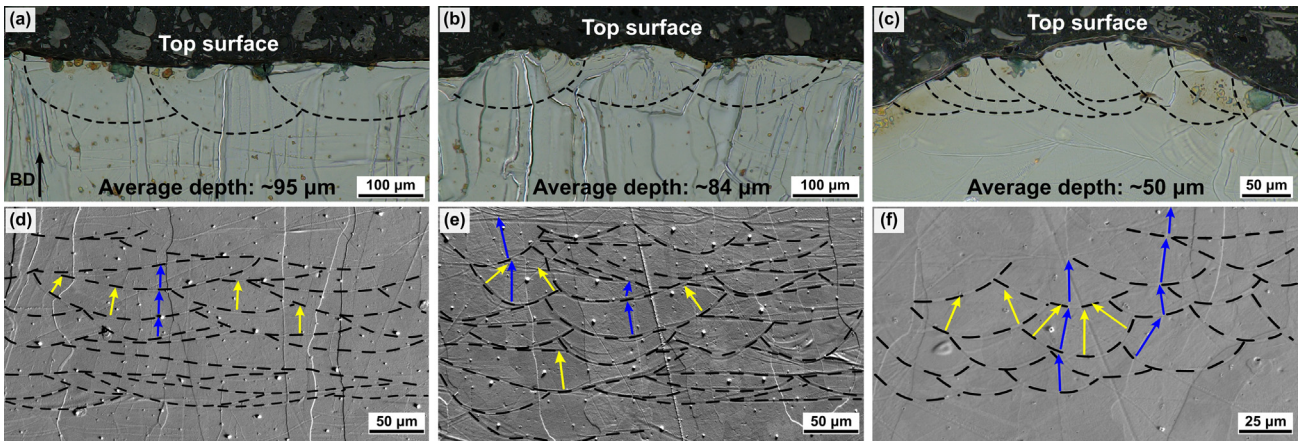


**Fig. 12.** Molten pool's side morphology of (a, d) S1, (b, e) S2, and (c, f) S3. (a)-(c) are the OM images at the top layer of the samples, and (d)-(f) are the SEM images, obtained from the middle of the samples.

**Table 3**
The average depth of molten pools and the proportion of remelting in S1-S3.

| Sample | Average depth (D) | Standard deviation | Proportion of remelting ($\frac{D-t}{D}$) |
|---|---|---|---|
| S1 | ~95 μm | ~4.3 μm | ~80% |
| S2 | ~84 μm | ~3.0 μm | ~76% |
| S3 | ~50 μm | ~6.7 μm | ~60% |

In the initial magnetization region, the magnetization is mainly completed by reversible domain wall movement. In addition to the intrinsic properties of the material, the microstructure is also a significant factor that affects this reversible domain wall movement and the corresponding permeability in this region. The presence of fewer defects (such as lower porosity and larger grain size), suitable texture, and lower residual stress will contribute to a higher permeability by reducing the resistance of the domain wall movement [12–14]. Therefore, S1 exhibits the highest permeability due to its lower number of pores, larger grain sizes, and more grains with their easy axis for magnetization parallel to H. Given that the microstructure features of S2 and S3 are relatively similar, they exhibit comparable magnetization curve in the initial magnetization region.

As we move to the irreversible domain wall movement region (i.e., domain growth region), a trend reversal is observed. It is likely that the microstructural features influenced the eddy current, which in turn affects the permeability at this stage. Eddy current produces a magnetic field opposite to H, resulting in the actual magnetic field applied in the testing ring samples being lower than the setting value. The value of the eddy current in this experiment is mainly influenced by three factors: (i) resistivity, (ii) length of the eddy current path, and (iii) AC frequency. Higher resistivity, shorter eddy current path, and lower AC frequency all contribute to a smaller eddy current. Resistivity generally decreases with increasing grain size and reduction in pores [67,68]. The presence of pores can divide the eddy current path into several smaller

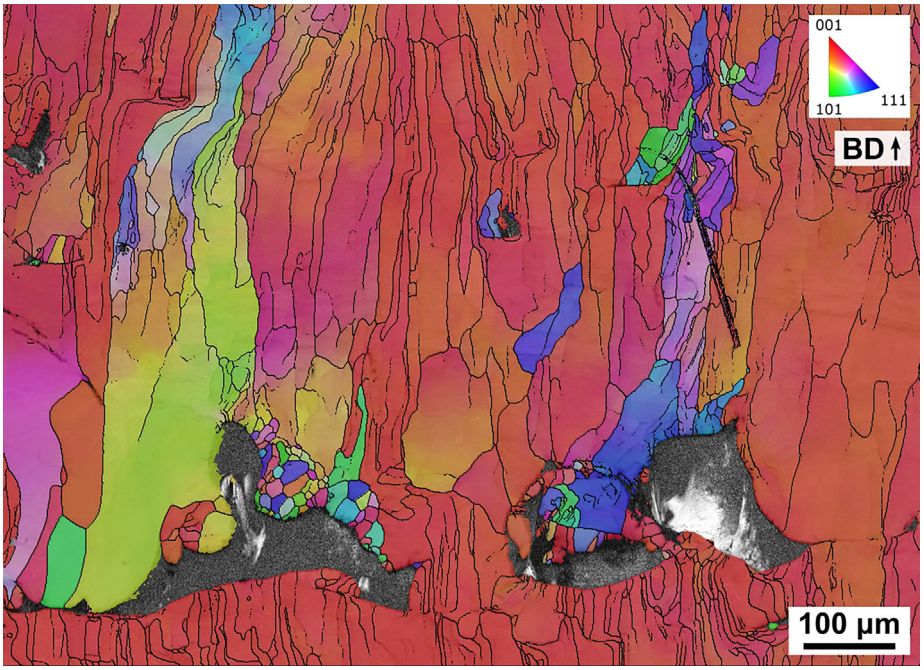


**Fig. 13.** EBSD image illustrating the interruption of epitaxial growth due to the presence of a lack-of-fusion defect, which is highlighted through IPF-BD coloring.

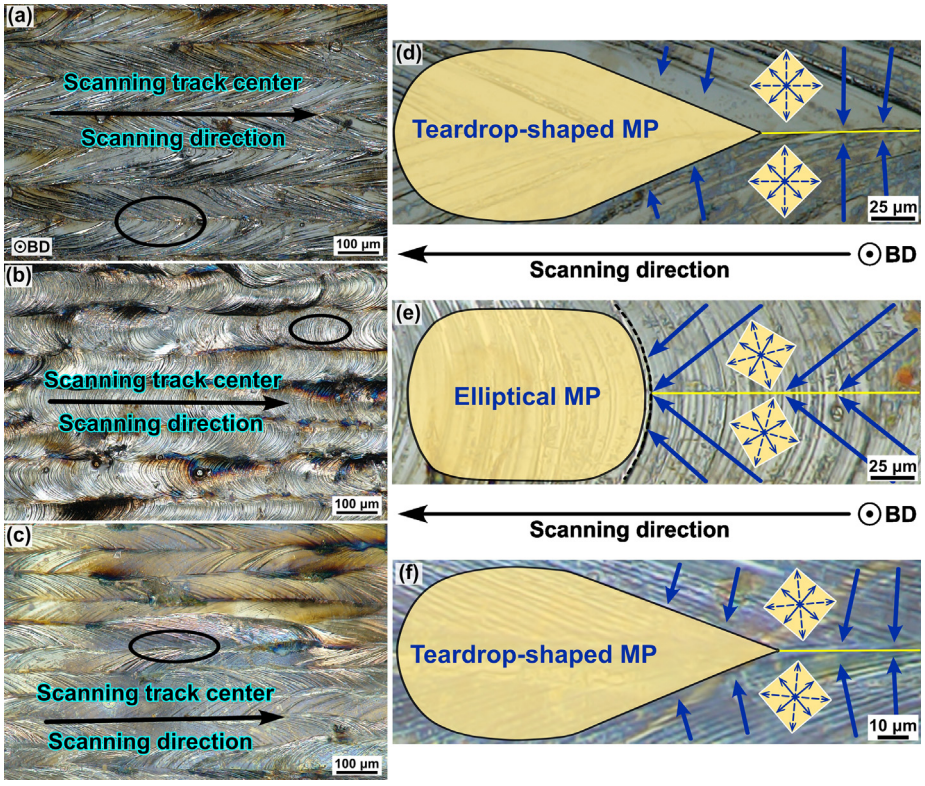


**Fig. 14.** (a)-(c) are the OM images showing the top morphology of the molten pool in S1-S3, respectively. (d)-(f) show the molten pool schematic (i.e., teardrop- and elliptical-shaped) of S1-S3, respectively. The squares in (d)-(f) are the representative orientation of grains contributing to the θ-fiber texture in the molten pool.

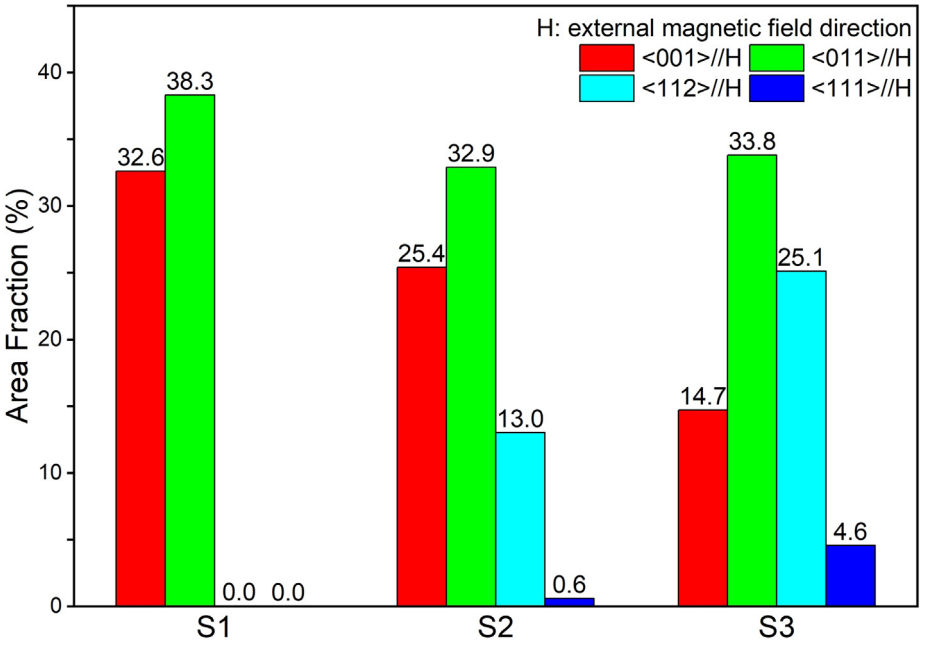


**Fig. 15.** The statistics of the area fraction of each crystal orientation parallel to H in Fig. 5 (a)-(c).

loops, reducing the eddy current by decreasing the length of the current path. Consequently, the eddy current in the samples decreases from S1 to S3. The eddy current's influences in the initial magnetization region are not obvious when the external magnetic field is small. However, with a continuous increase in the external magnetic field, the eddy current increases, and its influence becomes significant. Thus, the inverse relationship of S1-S3 is observed in the domain growth region. This inverse relationship becoming more apparent with increasing AC frequency serves as indirect evidence that the eddy current is responsible.

In the domain rotation region, domain wall movement does not occur, and thus, the relationship between the driven force and resistance of domain wall movement need not be considered. The magnetic flux density in this region depends on the alignment

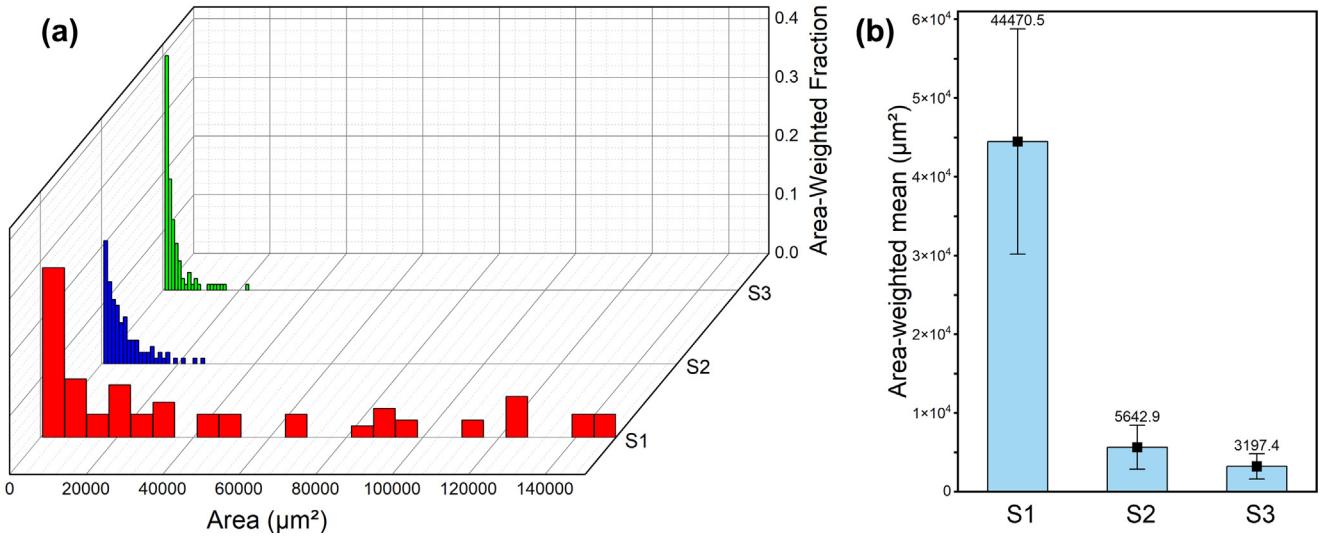


**Fig. 16.** (a) The grains size distribution of S1-S3, which is counted from Fig. 3, and (b) the relative area-weighted mean with the standard deviation of grain size of S1- S3.

degree between H and the easy/hard axis of magnetization in the samples. Therefore, S1, with the most ⟨001⟩//H and no ⟨111⟩//H, exhibits the highest magnetic flux density and permeability. Conversely, S3, with the least ⟨001⟩//H and the most ⟨111⟩//H, exhibits the poorest performance.

In summary, S1 exhibits the best overall magnetic performance due to its favorable conditions for magnetic properties, such as fewer defects (i.e., fewer pores and larger grain size) and more grains with the easy axis parallel to H. However, it should be noted that the magnetic properties of the as-built samples are greatly affected, negatively, by residual stress and dislocation density, which are considerably high (see Fig. S7). This could be the reason that S1′s magnetic performance still falls short of commercial products [69]. Therefore, future plans include performing heat treatment to reduce dislocations and residual stress.

## 5. Conclusions

In this research, the different microstructure (especially texture) of LPBFed Fe3.5Si (wt. %) was obtained by controlling the processing parameters, where samples S1 and S3 could be considered near grain-oriented and near non-oriented electric steels, respectively. The detailed texture features of these samples were analyzed, and their magnetic properties were measured with the AC method and compared. According to the results, it was concluded that:

(1) With constant VED, the side and top morphologies of molten pools are determined by different laser scanning parameters. For the side morphology, with the reduction of LED and laser power, molten pools will change from large, flat, and well-overlapped (S1) to small, protuberant, and less overlapped (S3). For the top morphology, fast scanning speed will produce a tear-drop molten pool (S1 and S3), while the opposite will yield an elliptical molten pool (S2).
(2) The texture feature is related to both side and top morphologies of molten pools. For the out-of-plane texture feature, large, low aspect ratio, and well-overlapped molten pools yielded strong ⟨001⟩//BD texture with a strong columnar feature (seen in S1 samples with high laser power and LED). While small, unstable, and less overlapped molten pools tend to form a near-random distribution of grains orientation with no obvious columnar feature. Porosity ensues as a by-product of unstable molten pools. For the in-plane texture feature, when the straight trailing molten pool boundaries of teardrop-shaped molten pools change to curved molten pool boundaries of the elliptical molten pools, the angle between the ⟨001⟩ in θ-fiber texture and SD will shift from around 45° to around 30°, and the major axis of grain rotates from perpendicular to SD to closer to SD.
(3) Samples with fewer defects, including larger grain size and fewer pores, as well as a higher area fraction of ⟨001⟩//H, generally displayed a larger amplitude permeability ($\mu_a$) and maximum magnetic flux density ($B_m$), but also a higher coercivity ($H_c$) and power loss ($P_s$) when subjected to external magnetization in the direction of H. However, the beneficial effect of these microstructure features on magnetic properties may be limited by the presence of residual stress and high dislocation density within the as-built samples.

These results found in this paper could guide to form suitable texture within the motor structure, and hence providing potential methods to improve motor performances. Furthermore, future research work will be necessary to supplement three things. One is that there are more pores inside S3, thus, how to obtain the near non-oriented microstructure with relatively low porosity needs to be studied. The other is that since the magnetic properties of these samples are worse than the commercial products, further annealing is necessary, where investigating how these three kinds of fiber textures and relative magnetic properties evolve during different annealing processes (i.e., removing residual stress and recrystallization) will be important. Finally, to achieve better-textured specimens in both out-of-plane and in-plane orientations, it is necessary to explore the texture evolution with respect to SD, as well as after heat treatment procedures.

## CRediT authorship contribution statement

**Fanbo Meng:** Writing – original draft, Conceptualization, Methodology, Validation, Investigation. **Sheng Huang:** Supervision, Conceptualization, Writing – review & editing. **Kwang Boon Lau:** Investigation. **You Zhou:** Writing – review & editing. **Yuheng Deng:** Investigation. **Pei Wang:** Writing – review & editing. **Xiaojun Shen:** Writing – review & editing. **Christopher H.T. Lee:** Writing – review & editing, Supervision, Funding acquisition.

## Data availability

Data will be made available on request.

## Declaration of Competing Interest

The authors declare that they have no known competing financial interests or personal relationships that could have appeared to influence the work reported in this paper.

## Acknowledgments

This work was supported by National Research Foundation (NRF) Singapore under its NRF Fellowship Grant NRF-NRFF12-2020-0003; the Agency for Science, Technology and Research (A*STAR) of Singapore via the Structural Metal Alloys Programme (No. A18B1b0061); and the Individual Research Grant (Grant reference No. A20E7c0109) of the Agency for Science, Technology and Research of Singapore.

## Appendix A. Supplementary data

Supplementary data to this article can be found online at https://doi.org/10.1016/j.matdes.2023.112037.

## References

[1] S. Cai, J.L. Kirtley, C.H.T. Lee, Critical Review of Direct-Drive Electrical Machine Systems for Electric and Hybrid Electric Vehicles, IEEE Trans. Energy Convers. 37 (2022) 2657–2668, https://doi.org/10.1109/TEC.2022.3197351.
[2] C.H.T. Lee, W. Hua, T. Long, C. Jiang, L.V. Iyer, A Critical Review of Emerging Technologies for Electric and Hybrid Vehicles, IEEE Open J. Veh. Technol. 2 (2021) 471–485, https://doi.org/10.1109/OJVT.2021.3138894.
[3] C. Liu, K.T. Chau, C.H.T. Lee, Z. Song, A Critical Review of Advanced Electric Machines and Control Strategies for Electric Vehicles, Proc. IEEE 109 (2021) 1004–1028, https://doi.org/10.1109/JPROC.2020.3041417.
[4] R. Wrobel, B. Mecrow, A Comprehensive Review of Additive Manufacturing in Construction of Electrical Machines, IEEE Trans. Energy Convers. 35 (2020) 1054–1064, https://doi.org/10.1109/TEC.2020.2964942.
[5] S. Madichetty, S. Mishra, M. Basu, New trends in electric motors and selection for electric vehicle propulsion systems, IET Electr. Syst. Transp. 11 (2021) 186–199, https://doi.org/10.1049/els2.12018.
[6] F. Wu, A.M. EL-Refaie,, Toward Additively Manufactured Electrical Machines: Opportunities and Challenges, IEEE Trans. Ind. Appl. 56 (2020) 1306–1320, https://doi.org/10.1109/TIA.2019.2960250.
[7] M.S.K.K.Y. Nartu, S. Dasari, A. Sharma, S.A. Mantri, S. Sharma, M.V. Pantawane, B. McWilliams, K. Cho, N.B. Dahotre, R. Banerjee, Omega versus alpha precipitation mediated by process parameters in additively manufactured high strength Ti–1Al–8V–5Fe alloy and its impact on mechanical properties, Mater. Sci. Eng. A 821 (2021), https://doi.org/10.1016/j.msea.2021.141627 141627.
[8] S.L. Sing, W.Y. Yeong, Laser powder bed fusion for metal additive manufacturing: perspectives on recent developments, Virtual Phys. Prototyp. 15 (2020) 359–370, https://doi.org/10.1080/17452759.2020.1779999.
[9] T. DebRoy, H.L. Wei, J.S. Zuback, T. Mukherjee, J.W. Elmer, J.O. Milewski, A.M. Beese, A. Wilson-Heid, A. De, W. Zhang, Additive manufacturing of metallic components – Process, structure and properties, Prog. Mater. Sci. 92 (2018) 112–224, https://doi.org/10.1016/j.pmatsci.2017.10.001.
[10] A. du Plessis, S.M.J. Razavi, M. Benedetti, S. Murchio, M. Leary, M. Watson, D. Bhate, F. Berto, Properties and applications of additively manufactured metallic cellular materials: A review, Prog. Mater. Sci. 125 (2022), https://doi.org/10.1016/j.pmatsci.2021.100918 100918.
[11] J. Fan, L. Zhang, S. Wei, Z. Zhang, S.-K. Choi, B. Song, Y. Shi, A review of additive manufacturing of metamaterials and developing trends, Mater. Today 50 (2021) 303–328, https://doi.org/10.1016/j.mattod.2021.04.019.
[12] M.E. McHenry, D.E. Laughlin, Magnetic Properties of Metals and Alloys, in: Phys. Metall., Elsevier, 2014: pp. 1881–2008. 10.1016/B978-0-444-53770-6.00019-8.
[13] F. Fiorillo, G. Bertotti, C. Appino, M. Pasquale, Soft Magnetic Materials, in: Wiley Encycl. Electr. Electron. Eng., John Wiley & Sons, Inc., Hoboken, NJ, USA, 1999: pp. 1–42. 10.1002/047134608X.W4504.pub2.
[14] C.-W. Chen, Magnetism and metallurgy of soft magnetic materials, Courier Corporation, 2013.
[15] S. Li, K.B. Lau, D. Wuu, F. Wei, M. Lin, A. Cheong, P. Wang, C.C. Tan, U. Ramamurty, 3D printing of ductile equiatomic Fe-Co alloy for soft magnetic applications, Addit. Manuf. 47 (2021), https://doi.org/10.1016/j.addma.2021.102291 102291.
[16] K.A. Liogas, K.B. Lau, Z. Wang, D.N. Brown, E. Polatidis, P. Wang, A.M. Korsunsky, Effect of heat treatment on the microstructure and magnetic properties of laser powder bed fusion processed equiatomic Co-Fe, Addit. Manuf. 67 (2023), https://doi.org/10.1016/j.addma.2023.103499 103499.
[17] D. Xue, G. Chai, X. Li, X. Fan, Effects of grain size distribution on coercivity and permeability of ferromagnets, J. Magn. Magn. Mater. 320 (2008) 1541–1543, https://doi.org/10.1016/j.jmmm.2008.01.004.
[18] G. Herzer, Grain structure and magnetism of nanocrystalline ferromagnets, IEEE Trans. Magn. 25 (1989) 3327–3329, https://doi.org/10.1109/20.42292.
[19] G. Herzer, Grain size dependence of coercivity and permeability in nanocrystalline ferromagnets, IEEE Trans. Magn. 26 (1990) 1397–1402, https://doi.org/10.1109/20.104389.
[20] G. Herzer, Soft magnetic nanocrystalline materials, Scr. Metall. Mater. 33 (1995) 1741–1756, https://doi.org/10.1016/0956-716X(95)00397-E.
[21] G. Herzer, Anisotropies in soft magnetic nanocrystalline alloys, J. Magn. Magn. Mater. 294 (2005) 99–106, https://doi.org/10.1016/j.jmmm.2005.03.020.
[22] T.N. Lamichhane, L. Sethuraman, A. Dalagan, H. Wang, J. Keller, M.P. Paranthaman, Additive manufacturing of soft magnets for electrical machines—a review, Mater. Today Phys. 15 (2020), https://doi.org/10.1016/j.mtphys.2020.100255 100255.
[23] A. Krings, A. Boglietti, A. Cavagnino, S. Sprague, Soft Magnetic Material Status and Trends in Electric Machines, IEEE Trans. Ind. Electron. 64 (2017) 2405–2414, https://doi.org/10.1109/TIE.2016.2613844.
[24] J.M. Silveyra, E. Ferrara, D.L. Huber, T.C. Monson, Soft magnetic materials for a sustainable and electrified world, Science 362 (2018) eaao0195, https://doi.org/10.1126/science.aao0195.
[25] N. Sanaei, A. Fatemi, Defects in additive manufactured metals and their effect on fatigue performance: A state-of-the-art review, Prog. Mater. Sci. 117 (2021), https://doi.org/10.1016/j.pmatsci.2020.100724 100724.
[26] T.H. Becker, P. Kumar, U. Ramamurty, Fracture and fatigue in additively manufactured metals, Acta Mater. 219 (2021), https://doi.org/10.1016/j.actamat.2021.117240 117240.
[27] C. Tan, F. Weng, S. Sui, Y. Chew, G. Bi, Progress and perspectives in laser additive manufacturing of key aeroengine materials, Int. J. Mach. Tools Manuf. 170 (2021), https://doi.org/10.1016/j.ijmachtools.2021.103804 103804.
[28] B.A. AlMangour, Additive Manufacturing of High-Performance 316L Stainless Steel Nanocomposites via Selective Laser Melting, Ph.D., n.d. https://www.proquest.com/docview/1914920700/abstract/D78545687CBE4D2FPQ/1 (accessed February 22, 2022).
[29] F. Bartolomeu, M. Buciumeanu, E. Pinto, N. Alves, O. Carvalho, F.S. Silva, G. Miranda, 316L stainless steel mechanical and tribological behavior—A comparison between selective laser melting, hot pressing and conventional casting, Addit. Manuf. 16 (2017) 81–89, https://doi.org/10.1016/j.addma.2017.05.007.
[30] J.-P. Choi, G.-H. Shin, M. Brochu, Y.-J. Kim, S.-S. Yang, K.-T. Kim, D.-Y. Yang, C.-W. Lee, J.-H. Yu, Densification Behavior of 316L Stainless Steel Parts Fabricated by Selective Laser Melting by Variation in Laser Energy Density, Mater. Trans. 57 (2016) 1952–1959, https://doi.org/10.2320/matertrans.M2016284.
[31] B. Cheng, F. Wei, W.H. Teh, J.J. Lee, T.L. Meng, K.B. Lau, L.T. Chew, Z. Zhang, K.H. Cheong, C.K. Ng, P. Wang, C.C. Tan, U. Ramamurty, Ambient pressure fabrication of Ni-free high nitrogen austenitic stainless steel using laser powder bed fusion method, Addit. Manuf. 55 (2022), https://doi.org/10.1016/j.addma.2022.102810 102810.
[32] E. Liverani, S. Toschi, L. Ceschini, A. Fortunato, Effect of selective laser melting (SLM) process parameters on microstructure and mechanical properties of 316L austenitic stainless steel, J. Mater. Process. Technol. 249 (2017) 255–263, https://doi.org/10.1016/j.jmatprotec.2017.05.042.
[33] D. Wang, C. Song, Y. Yang, Y. Bai, Investigation of crystal growth mechanism during selective laser melting and mechanical property characterization of 316L stainless steel parts, Mater. Des. 100 (2016) 291–299, https://doi.org/10.1016/j.matdes.2016.03.111.
[34] W.M. Tucho, V.H. Lysne, H. Austbø, A. Sjolyst-Kverneland, V. Hansen, Investigation of effects of process parameters on microstructure and hardness of SLM manufactured SS316L, J. Alloys Compd. 740 (2018) 910–925, https://doi.org/10.1016/j.jallcom.2018.01.098.
[35] S. Dryepondt, P. Nandwana, P. Fernandez-Zelaia, F. List, Microstructure and high temperature tensile properties of 316L fabricated by laser powder-bed fusion, Addit. Manuf. 37 (2021), https://doi.org/10.1016/j.addma.2020.101723 101723.
[36] Y. Zhang, S. Zhang, Z. Zou, Y. Shi, Achieving an ideal combination of strength and plasticity in additive manufactured Ti–6.5Al–2Zr–1Mo–1V alloy through the development of tri-modal microstructure, Mater. Sci. Eng. A. 840 (2022), https://doi.org/10.1016/j.msea.2022.142944 142944.
[37] Z. Wang, Z. Xiao, Y. Tse, C. Huang, W. Zhang, Optimization of processing parameters and establishment of a relationship between microstructure and mechanical properties of SLM titanium alloy, Opt. Laser Technol. 112 (2019) 159–167, https://doi.org/10.1016/j.optlastec.2018.11.014.
[38] S. Huang, R.L. Narayan, J.H.K. Tan, S.L. Sing, W.Y. Yeong, Resolving the porosity-unmelted inclusion dilemma during in-situ alloying of Ti34Nb via laser powder bed fusion, Acta Mater. 204 (2021), https://doi.org/10.1016/j.actamat.2020.116522 116522.
[39] R.A. Michi, K. Sisco, S. Bahl, Y. Yang, J.D. Poplawsky, L.F. Allard, R.R. Dehoff, A. Plotkowski, A. Shyam, A creep-resistant additively manufactured Al-Ce-Ni-Mn alloy, Acta Mater. 227 (2022), https://doi.org/10.1016/j.actamat.2022.117699 117699.

[40] S. Wu, Z. Lei, B. Li, J. Liang, Y. Chen, Hot cracking evolution and formation mechanism in 2195 Al-Li alloy printed by laser powder bed fusion, Addit. Manuf. 54 (2022), https://doi.org/10.1016/j.addma.2022.102762 102762.
[41] C.N. Kuo, C.K. Chua, P.C. Peng, Y.W. Chen, S.L. Sing, S. Huang, Y.L. Su, Microstructure evolution and mechanical property response via 3D printing parameter development of Al–Sc alloy, Virtual Phys. Prototyp. 15 (2020) 120–129, https://doi.org/10.1080/17452759.2019.1698967.
[42] N.T. Aboulkhair, I. Maskery, C. Tuck, I. Ashcroft, N.M. Everitt, The microstructure and mechanical properties of selectively laser melted AlSi10Mg: The effect of a conventional T6-like heat treatment, Mater. Sci. Eng. A. 667 (2016) 139–146, https://doi.org/10.1016/j.msea.2016.04.092.
[43] Hiperco_50A_Alloy_(E199).pdf, (n.d.). https://f.hubspotusercontent20.net/hubfs/7407327/carpenter_electrification/Resources/Datasheets/Hiperco_50A_Alloy_(E199).pdf (accessed April 24, 2023).
[44] Downloads | VAC, (n.d.). https://vacuumschmelze.de/shared/quickNav/Downloads (accessed April 24, 2023).
[45] M. Garibaldi, I. Ashcroft, M. Simonelli, R. Hague, Metallurgy of high-silicon steel parts produced using Selective Laser Melting, Acta Mater. 110 (2016) 207–216, https://doi.org/10.1016/j.actamat.2016.03.037.
[46] M. Garibaldi, I. Ashcroft, N. Hillier, S.A.C. Harmon, R. Hague, Relationship between laser energy input, microstructures and magnetic properties of selective laser melted Fe-6.9%wt Si soft magnets, Mater. Charact. 143 (2018) 144–151, https://doi.org/10.1016/j.matchar.2018.01.016.
[47] S. Gao, X. Yan, C. Chang, Eric, Aubry, M. Liu, H. Liao, N. Fenineche, Effect of Laser Energy Density on Surface Morphology, Microstructure, and Magnetic Properties of Selective Laser Melted Fe-3wt.% Si Alloys, J. Mater. Eng. Perform. 30 (7) (2021) 5020–5030.
[48] A. Plotkowski, K. Carver, F. List, J. Pries, Z. Li, A.M. Rossy, D. Leonard, Design and performance of an additively manufactured high-Si transformer core, Mater. Des. 194 (2020), https://doi.org/10.1016/j.matdes.2020.108894 108894.
[49] A. Plotkowski, J. Pries, F. List, P. Nandwana, B. Stump, K. Carver, R.R. Dehoff, Influence of scan pattern and geometry on the microstructure and soft-magnetic performance of additively manufactured Fe-Si, Addit. Manuf. 29 (2019), https://doi.org/10.1016/j.addma.2019.100781 100781.
[50] H. Liu, Z. Liu, G. Cao, C. Li, G. Wang, Microstructure and texture evolution of strip casting 3wt% Si non-oriented silicon steel with columnar structure, J. Magn. Magn. Mater. 323 (2011) 2648–2651, https://doi.org/10.1016/j.jmmm.2011.06.002.
[51] H. Liu, Z. Liu, C. Li, G. Cao, G. Wang, Solidification structure and crystallographic texture of strip casting 3wt.% Si non-oriented silicon steel, Mater. Charact. 62 (2011) 463–468, https://doi.org/10.1016/j.matchar.2011.02.010.
[52] H.-Y. Song, H.-T. Liu, H.-H. Lu, H.-Z. Li, W.-Q. Liu, X.-M. Zhang, G.-D. Wang, Effect of hot rolling reduction on microstructure, texture and ductility of strip-cast grain-oriented silicon steel with different solidification structures, Mater. Sci. Eng. A. 605 (2014) 260–269, https://doi.org/10.1016/j.msea.2014.03.052.
[53] Z. Zhang, W. Wang, H. Fu, J. Xie, Effect of quench cooling rate on residual stress, microstructure and mechanical property of an Fe–6.5Si alloy, Mater. Sci. Eng. A. 530 (2011) 519–524, https://doi.org/10.1016/j.msea.2011.10.013.
[54] K.M. Lee, S.Y. Park, M.Y. Huh, J.S. Kim, O. Engler, Effect of texture and grain size on magnetic flux density and core loss in non-oriented electrical steel containing 3.15% Si, J. Magn. Magn. Mater. 354 (2014) 324–332, https://doi.org/10.1016/j.jmmm.2013.11.030.
[55] J. Qin, P. Yang, W. Mao, F. Ye, Effect of texture and grain size on the magnetic flux density and core loss of cold-rolled high silicon steel sheets, J. Magn. Magn. Mater. 393 (2015) 537–543, https://doi.org/10.1016/j.jmmm.2015.06.032.
[56] Y.-X. Zhang, M.-F. Lan, Y. Wang, F. Fang, X. Lu, G. Yuan, R.D.K. Misra, G.-D. Wang, Microstructure and texture evolution of thin-gauge non-oriented silicon steel with high permeability produced by twin-roll strip casting, Mater. Charact. 150 (2019) 118–127, https://doi.org/10.1016/j.matchar.2019.02.001.
[57] Y.H. Sha, C. Sun, F. Zhang, D. Patel, X. Chen, S.R. Kalidindi, L. Zuo, Strong cube recrystallization texture in silicon steel by twin-roll casting process, Acta Mater. 76 (2014) 106–117, https://doi.org/10.1016/j.actamat.2014.05.020.
[58] H. Jiao, Y. Xu, L. Zhao, R.D.K. Misra, Y. Tang, D. Liu, Y. Hu, M. Zhao, M. Shen, Texture evolution in twin-roll strip cast non-oriented electrical steel with strong Cube and Goss texture, Acta Mater. 199 (2020) 311–325, https://doi.org/10.1016/j.actamat.2020.08.048.
[59] L. Thijs, F. Verhaeghe, T. Craeghs, J.V. Humbeeck, J.-P. Kruth, A study of the microstructural evolution during selective laser melting of Ti–6Al–4V, Acta Mater. 58 (2010) 3303–3312, https://doi.org/10.1016/j.actamat.2010.02.004.
[60] Z. Sun, X. Tan, S.B. Tor, W.Y. Yeong, Selective laser melting of stainless steel 316L with low porosity and high build rates, Mater. Des. 104 (2016) 197–204, https://doi.org/10.1016/j.matdes.2016.05.035.
[61] T. Mishurova, K. Artzt, J. Haubrich, G. Requena, G. Bruno, New aspects about the search for the most relevant parameters optimizing SLM materials, Addit. Manuf. 25 (2019) 325–334, https://doi.org/10.1016/j.addma.2018.11.023.
[62] S. Huang, P. Kumar, W.Y. Yeong, R.L. Narayan, U. Ramamurty, Fracture behavior of laser powder bed fusion fabricated Ti41Nb via in-situ alloying, Acta Mater. 225 (2022), https://doi.org/10.1016/j.actamat.2021.117593 117593.
[63] A06 Committee, Test Method for Alternating-Current Magnetic Properties of Toroidal Core Specimens Using the Voltmeter-Ammeter-Wattmeter Method, ASTM International, n.d. 10.1520/A0927_A0927M-11.
[64] D. Chateigner, L. Lutterotti, M. Morales, Quantitative texture analysis and combined analysis, in (2019) 555–580, https://doi.org/10.1107/9780955360206000968.
[65] S. Kou, Welding metallurgy, 2nd ed., Wiley-Interscience, Hoboken, N.J., 2003.
[66] N. Kang, Q. Li, M.E. Mansori, B. Yao, F. Ma, X. Lin, H. Liao, Laser Powder Bed Fusion Processing of Soft Magnetic Fe–Ni–Si Alloys: Effect of Hot Isostatic Pressing Treatment, Chin. J. Mech. Eng. Addit. Manuf. Front. 1 (2022), https://doi.org/10.1016/j.cjmeam.2022.100054 100054.
[67] I. Bakonyi, Accounting for the resistivity contribution of grain boundaries in metals: critical analysis of reported experimental and theoretical data for Ni and Cu, Eur. Phys. J. Plus. 136 (2021) 410, https://doi.org/10.1140/epjp/s13360-021-01303-4.
[68] M. Apreutesei, C. Lopes, J. Borges, F. Vaz, F. Macedo, Modulated IR radiometry for determining thermal properties and basic characteristics of titanium thin films, J. Vac. Sci. Technol. Vac. Surf. Films. 32 (2014), https://doi.org/10.1116/1.4884351 041511.
[69] J.S. Corporation, ELECTRICAL STEEL SHEETS, (n.d.).